

# Micromechanical Resonators Based on Silicon Two-Dimensional Phononic Crystals of Square Lattice

Nan Wang, *Student Member, IEEE*, Julius Ming-Lin Tsai, Fu-Li Hsiao, Bo Woon Soon, Dim-Lee Kwong, *Fellow, IEEE*, Moorthi Palaniapan, and Chengkuo Lee, *Member, IEEE*

**Abstract**—Phononic crystal (PnC) resonators of Bloch-mode resonance made by replacing periodically arranged two or three rows of air holes with one row of air holes on a two-dimensional (2-D) silicon slab with air holes of square lattice have been investigated. Piezoelectric aluminum nitride (AlN) film is employed as the interdigital transducers to transmit and detect acoustic waves, thus making the whole microfabrication process CMOS compatible. We also fabricate a PnC structure which has a stopband of  $140 \text{ MHz} < f < 195 \text{ MHz}$  which agrees well with the simulation results. From our experimental results, we found that the two kinds of microfabricated PnC resonators have different optimization conditions in terms of resonant frequency and Q factor, as well as insertion loss, despite their similar design approach. As compared to PnC resonators of hexagonal lattice, the proposed Bloch-mode PnC resonators of square lattice demonstrated higher resonant frequency, higher Q factor, and a smaller device area. The promising acoustic characteristics may be further optimized for applications such as microfluidics, biomedical devices, and radio-frequency communications in the gigahertz range.

[2011-0059]

**Index Terms**—CMOS compatible, microelectromechanical systems (MEMS), phononic crystal (PnC), resonator.

## I. INTRODUCTION

ONE OF THE KEY components in radio frequency (RF) communication devices is the frequency reference oscillator. Due to the incompatibility of quartz crystals, which,

Manuscript received March 2, 2011; revised August 22, 2011; accepted October 10, 2011. Date of publication December 6, 2011; date of current version July 27, 2012. This work was supported in part by the Agency for Science, Technology and Research under Science and Engineering Research Council Grants 1021010022 and 1021650084 and in part by the National University of Singapore under Grant R263000598112. The work of N. Wang was supported by National University of Singapore under a Ph.D. scholarship grant. Subject Editor D. Elata.

N. Wang and B. W. Soon are with the Institute of Microelectronics, Agency for Science, Technology and Research, Singapore 117685, and also with the Department of Electrical and Computer Engineering, National University of Singapore, Singapore 117576 (e-mail: nan.wang@nus.edu.sg).

J. M.-L. Tsai and D.-L. Kwong are with the Institute of Microelectronics, Agency for Science, Technology and Research, Singapore 117685 (e-mail: tsaiml@ime.a-star.edu.sg; kwongdl@ime.a-star.edu.sg).

F.-L. Hsiao is with the Department of Electrical and Computer Engineering, National University of Singapore, Singapore 117576, and also with the Graduate Institute of Photonics, National Changhua University of Education, Changhua 500, Taiwan (e-mail: fulihhsiao@gmail.com).

M. Palaniapan and C. Lee are with the Department of Electrical and Computer Engineering, National University of Singapore, Singapore 117576 (e-mail: elemp@nus.edu.sg; elelc@nus.edu.sg).

Color versions of one or more of the figures in this paper are available online at <http://ieeexplore.ieee.org>.

Digital Object Identifier 10.1109/JMEMS.2011.2174416

currently, most reference oscillators are based on, with IC fabrication, silicon-integrated micromechanical oscillators are gaining more research interest due to the ability to be integrated with electronics [1]. Currently, researchers are mainly focusing on two types of microresonator technology, namely, capacitive-based [2]–[7] and piezoelectric-based [8]–[10] devices. However, there is a tradeoff between these two types of devices, which is known as the tradeoff between Q factor and motional impedance. For silicon micromechanical reference oscillators which are based on capacitive microelectromechanical systems resonators, researchers have already demonstrated an f-Q product as high as  $2 \times 10^{13}$  [11]. However, the motional impedance is also very high due to weak capacitive electroacoustic coupling. On the other hand, although piezoelectric-based microresonators can have their motional impedance to be below  $50 \Omega$ , the Q factor cannot be very high due to high loss in the piezoelectric materials [10].

Phononic crystal (PnC) is a potential candidate to overcome the tradeoff between Q factor and motional impedance as PnC can store elastic energy in the microcavity made on high-Q materials such as silicon [12]. PnCs are the acoustic wave equivalent of photonic crystals (PhCs), which consist of periodically arranged scattering centers embedded in a homogeneous background matrix. From the aspect of elastic properties, PnCs are inhomogeneous materials with periodic variations. Thus, the dispersion characteristics of the PnCs lead to the existence of phononic bandgaps, in which the propagation of elastic waves within a certain frequency range is prohibited in any direction. PnCs with properly engineered bandgaps can be the basis of realizing a variety of functionalities such as acoustic waveguides, cavities, and filters. We can obtain such functionalities by modifying portions of the PnC structure for various applications in wireless communication and sensors.

So far, various types of acoustic and elastic wave propagation have been studied in different classes of PnC structures. Surface acoustic waves in semi-infinite PnCs with cylindrical air holes etched in a single material or a solid/solid composition whereby the air holes are filled with other kinds of materials have been studied [13], [14]. Recently, the guided waves in 2-D PnC slabs have attracted more attention due to the fact that the 2-D nature of PnC slabs can provide better confinement of elastic energy. Various configurations of PnC slabs, such as cylindrical air holes etched in freestanding membrane [15]–[17], cylindrical rods inserted into the air holes [14], [18], and cylindrical rods

deposited on the top of the membrane [19], as well as inverse acoustic bandgap (IABG) structure which is formed based on the use of high acoustic velocity center media (AlN and Pt) held by four thin tethers in a low acoustic velocity matrix (air) [20], have been proved to have phononic bandgaps for elastic waves traveling in any direction. Researchers have also demonstrated the PnC slabs which can be operated in gigahertz frequencies [21], [22], giving PnCs a big boost toward applications in RF communications.

By adding defects to PnC structure, devices of various functionalities like waveguides and resonators have been reported [18], [19], [23]–[30]. For example, a waveguide is formed by adding a line defect (e.g., removing one row of holes) to PnC structure [27]; waveguide-mode resonance can be obtained when the two ends of the waveguide are closed by adding air holes at the two ends [28]; cavity-mode resonator can be formed by adding either a point defect or a line defect in the form of a Fabry-Perot structure [31]. Also, waveguides are also demonstrated in IABG structure [32] to achieve ultrasonic focusing.

Generally, any wavelike phenomenon in a periodic medium can be described as Bloch wave. For example, a periodic dielectric in electromagnetism leads to PhCs, and a periodic acoustic medium leads to PnCs. Similar to the mechanism of forming photonic bandgap, phononic bandgap can be formed in phononic structure when scattering inclusions arranged periodically in a homogeneous host material which causes elastic waves in certain frequencies to be completely reflected by the structure. Researchers have already studied Bloch-mode resonance by modifying the periodicity of portions of the PhC to form a micro-/nanocavity [33]–[38], while slotted waveguide utilizing Bloch-mode resonance has been proved to have a higher Q factor and a lower insertion loss (IL) due to the better confinement of light inside the waveguide [39]–[41]. Conceptually, the micro-/nanocavity formed by modifying the periodicity of portions of the PhC is effectively a wavelength-scale Fabry-Perot cavity with PhC structures on both sides of the cavity, which functions like a mirror to reflect and thus trap the nanobeam waveguide mode. Because the cavity mode penetrates some distance into the mirror, it is crucial that the waveguide mode does not abruptly terminate at the PhC mirror boundary but penetrates and exponentially decays within the PhC structure, as abrupt termination would lead to substantial amount of scattering loss [34]. Thus, by analogy, the cavity-mode PnC resonator [31] is actually a Fabry-Perot structure which converts the Bloch waves from Bloch mode to propagating mode when the waves enter the cavity region from the surrounding PnC region. This mode conversion can lead to large amount of scattering loss, due to the large mismatch in acoustic impedance between these two regions. On the other hand, when defects are introduced to the PnC structure by replacing the central two or three rows of inclusions by only one row of inclusions, only the periodicity of Bloch waves is changed when the waves enter the cavity region from the surrounding PnC region, while the mode of the Bloch waves is still kept as Bloch mode. Thus, the mismatch in acoustic impedance can be reduced, and as a result, smaller amount of scattering loss and higher Q factor can be expected. In this pa-

per, we present the design, fabrication, and characterization of micromechanical PnC resonators using Bloch-mode resonance. PnC bandgap optimization is done by the finite-element method (FEM) because the width of the bandgap is inversely related to the critical dimension (CD) of the structure and small CD could be very challenging to the microfabrication capability. For the purpose of easy comparison, the thickness of the PnC structures is fixed at 10  $\mu\text{m}$ , and this is also the thickness of the device layer of the silicon-on-insulator (SOI) substrate used in later microfabrication. The transmission spectra of designed Bloch-mode PnC resonators are also analyzed using FEM, while experimental results of the microfabricated resonators using a 2-D silicon-based PnC slab with high-Q resonant peaks in the 100-MHz range are presented.

## II. MODELING AND DESIGN

### A. PnC Bandgap Optimization

The studies of the propagation of bulk waves in 2- or 3-D PnCs include the analysis of the bandgap effect in finite structures as well as the confinement and guiding of acoustic energy through the use of defect inclusions in the PnC structures. COMSOL Multiphysics software is employed for the modeling of the band structure of the 2-D PnC slab. The main principle behind the FEM of the band structure follows closely from first-principle physics, i.e., combination of Newton's second law of motion and a constitutive relation. The structural mechanics formulation is shown in

$$\rho \frac{\partial^2 u}{\partial t^2} - \nabla \cdot c \nabla u = F = 0. \quad (1)$$

In (1),  $u$  is the solution vector which consists of displacements  $u_x$ ,  $u_y$ , and  $u_z$ . In our study, we set  $F = 0$  because the solutions that we are looking for are the eigenvalues. Upon Fourier transform of (1), the resulting harmonic time dependence term  $\exp(i\omega t)$  can be factored out. The time derivative can then be replaced by  $-\omega^2$ , as shown in

$$\frac{\nabla \cdot c \nabla}{\rho} u = \omega^2 u. \quad (2)$$

As shown in (2), the mode frequencies can be derived from the eigenvalues  $\omega^2$ , which could be solved using FEM, with a unit cell (inset of Fig. 1) of the PnC structure constructed as the first step. Subdomain settings are then applied to simulate the structure of air holes in the silicon background. Periodic boundary conditions are applied along the  $x$ - and  $y$ -directions. Lastly, we combine all the eigenfrequencies computed by the eigenfrequency solver to generate the band structure. An optimized plot is shown in Fig. 1 as an example of such a band structure, where a phononic bandgap can be clearly observed. The detailed optimization process will be discussed later in this section.

As shown in the schematics drawing (inset of Fig. 1),  $a$  is the lattice constant (or pitch) which means the distance between the centers of two adjacent holes,  $d$  is the thickness of the PnC slab, and  $r$  is the radius of the air holes. According to the bandgap optimization done using full 3-D plane-wave-expansion technique

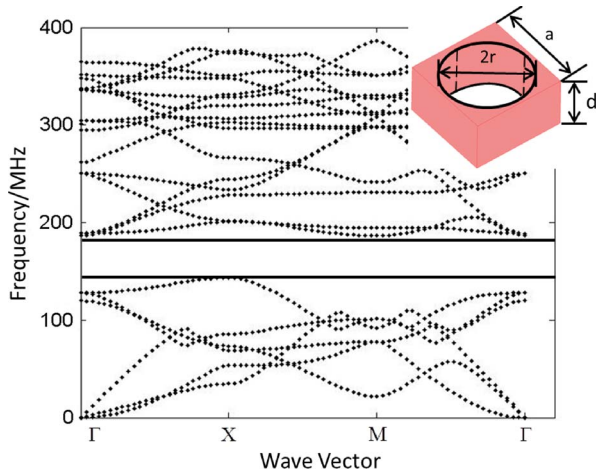


Fig. 1. Band structure of the PnC structure with  $d = 10 \mu\text{m}$ ,  $r = 8.18 \mu\text{m}$ , and  $a = 18.18 \mu\text{m}$ , which gives  $r/a = 0.45$  and  $d/a = 0.55$ . A unit cell of the structure is shown in the inset.

reported in [16], given the fixed thickness of  $d = 10 \mu\text{m}$ , the maximum bandgap can be achieved when  $a = 17.54 \mu\text{m}$ , which means  $d/a = 0.57$ , and maximum bandgap can be achieved when  $r/a = 0.47$ . However, this will render the diameter of air holes to be  $16.49 \mu\text{m}$ , if  $a$  is chosen to be  $17.54 \mu\text{m}$ . As a result, the minimum feature size (CD), which is the minimum width of silicon between two adjacent air holes in this case, is  $1.05 \mu\text{m}$ . Considering the feature size deviation attributed to fabrication process, e.g., the side wall profile variation of deep reactive ion etching (DRIE) process, such a small feature size brings significant challenge to microfabrication capability. Therefore, we set  $r = 8.18 \mu\text{m}$  and  $a = 18.18 \mu\text{m}$  as the targeted fabricated values. This gives us  $r/a = 0.45$ , which still yields a reasonably wide bandgap while making the microfabrication process less challenging. The calculated band structure after optimization shown in Fig. 1 has a stopband of  $143.3 \text{ MHz} < f < 186.3 \text{ MHz}$ , which renders the gap-to-midgap frequency ratio to be 26.1%.

### B. PnC Resonator Structure Design

After optimizing the band structure, the confinement and guiding of acoustic energy through the use of defect inclusions in the PnC structures are also analyzed using FEM. As inspired by the Bloch-mode resonance and the slotted waveguides created in PhCs, here, we design two different types of PnC Bloch-mode resonators which utilize defects in the PnC slab to generate resonant behavior [see Fig. 2(c) and (e)]. Fig. 2(a) shows the schematic drawing of a PnC. The first type of PnC Bloch-mode resonators that we designed is formed by removing two rows of air holes (cavity width  $w = 2a$ ) and replacing them with one row of air holes at the center [see Fig. 2(c)]. The second type of PnC Bloch-mode resonators is formed by removing three rows of air holes ( $w = 3a$ ) and replacing them with one row of air holes at the center [see Fig. 2(e)]. Structures with various radii of the central holes ( $r'$ ) are designed but only structures with  $r' = 4 \mu\text{m}$  are shown for the purpose of illustration. Fig. 2(a), (c), and (e) are the schematic drawings,

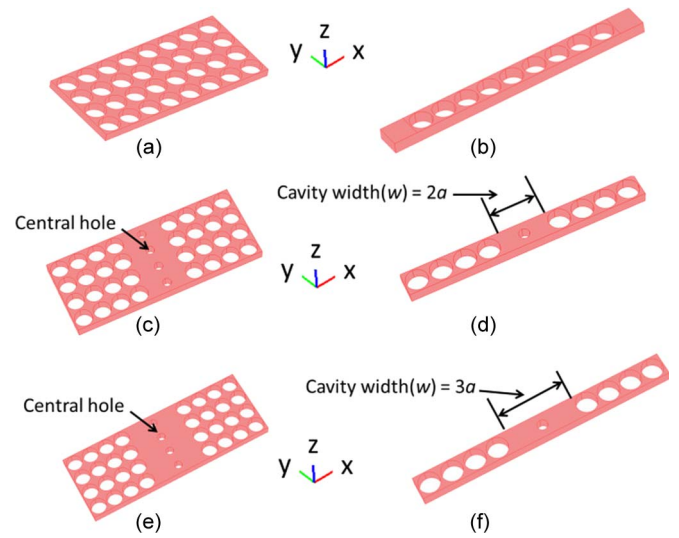


Fig. 2. Schematic drawings of (a) PnC structure, (b) repeating unit of the PnC structure, (c) PnC Bloch-mode resonator formed by removing two rows of PnC holes (cavity width  $w = 2a$ ) and replacing them with one row of PnC holes at the center, (d) repeating unit of PnC Bloch-mode resonator with  $w = 2a$ , (e) PnC Bloch-mode resonator formed by removing three rows of PnC holes (cavity width  $w = 3a$ ) and replacing them with one row of PnC holes at the center, and (f) repeating unit of PnC Bloch-mode resonator with  $w = 3a$ .

while Fig. 2(b), (d), and (f) are the repeating unit of each design for transmission simulation, respectively.

The transmission spectra of the designed PnC resonator structures are also analyzed by FEM, with a repeating unit of the PnC or any other PnC resonator structure [see Fig. 2(b), (d), and (f)] constructed first. A flat silicon plate without any PnC structure and with the same length of wave propagation is also constructed for the purpose of normalization. Periodic boundary conditions are then applied along the  $y$ -direction. In this paper, we only show the two cases of  $r' = 6 \mu\text{m}$  as examples [see Fig. 3(b) and (c)]. The transmission spectrum of the optimized PnC [see Fig. 3(a)] has a stopband of  $143.8 \text{ MHz} < f < 186.8 \text{ MHz}$ , which is in excellent agreement with the simulation data obtained by the eigenfrequency solver (see Fig. 1). The resonant frequencies of the two designed PnC resonators are comparable ( $162.75 \text{ MHz}$  for  $w = 2a$  and  $160.95 \text{ MHz}$  for  $w = 3a$ ), with the resonant frequency of the first design ( $w = 2a$  and  $r' = 6 \mu\text{m}$ ) being slightly higher, as shown in Fig. 3(b) and (c).

Using the same structures which were built for the analysis of resonant frequencies, we also analyzed the mode profiles of displacement in the  $x$ -,  $y$ -, and  $z$ -directions of all designed PnC resonators under their respective resonant frequencies. Again, periodic boundary conditions are applied along the  $y$ -direction. As elastic waves in the silicon plate propagate by the interactions among the silicon atoms when they are displaced from their equilibrium positions, the energy stored in any solid structure is then associated with the displacements of the silicon atoms within the silicon plate. Thus, by analyzing the displacements of all the silicon atoms within the silicon plate (mode profiles of displacement), we can get information about the energy distribution along the structure. Fig. 4 shows the mode profiles of displacement of the PnC Bloch-mode resonators with  $w = 2a$  and with (a)  $r' = 2 \mu\text{m}$ , (b)  $r' = 4 \mu\text{m}$ ,

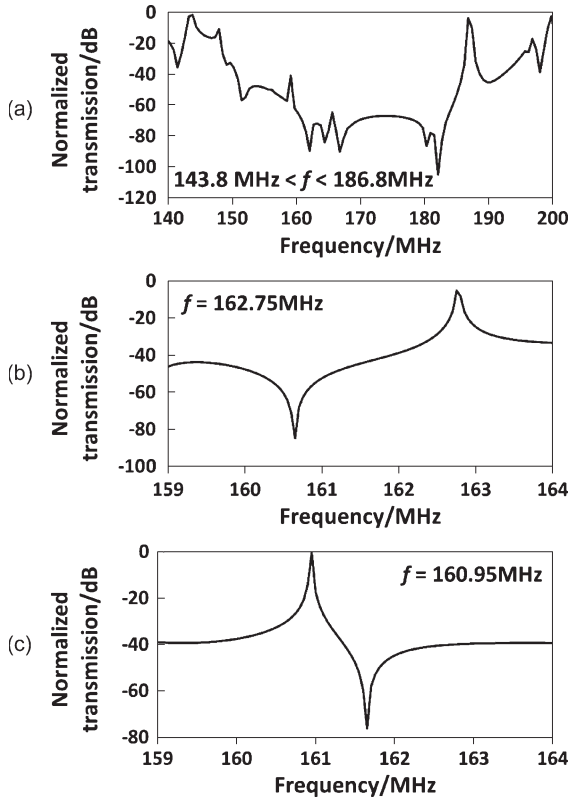


Fig. 3. Simulated transmission spectra of (a) PnC structure, (b) PnC Bloch-mode resonator with  $w = 2a$  and  $r' = 6 \mu\text{m}$ , and (c) PnC Bloch-mode resonator with  $w = 3a$  and  $r' = 6 \mu\text{m}$ .

(c)  $r' = 6 \mu\text{m}$ , and (d)  $r' = 8 \mu\text{m}$ , while Fig. 5 shows the mode profiles of displacement of the PnC Bloch-mode resonators with  $w = 3a$  and with (a)  $r' = 2 \mu\text{m}$ , (b)  $r' = 4 \mu\text{m}$ , (c)  $r' = 6 \mu\text{m}$ , and (d)  $r' = 8 \mu\text{m}$ . The  $u_1$ ,  $u_2$ , and  $u_3$  represent the displacement vector components in the  $x$ -,  $y$ -, and  $z$ -directions, respectively. The color bar indicates the amplitude of displacements in an arbitrary unit. For the cases whereby the displacement vector components in all three directions are concentrated at the central defect region [e.g., see Fig. 4(b)], which means the energy of the structure is concentrated at the central defect region, we can expect higher Q factors as a result of the better confinement of the energy by the phononic structure surrounding the central defect region. On the other hand, lower Q factors are expected for the cases whereby the displacement vector components are distributed evenly along the structure or concentrated at one end of the structure [e.g., see Fig. 5(d)]. For these cases, the energy is confined poorly in the central defect region, resulting in lower Q factors expected.

### III. MICROFABRICATION

To realize the 2-D PnC slab structure, first, the SOI wafer of the  $10\text{-}\mu\text{m}$  device layer with  $1\text{-}\mu\text{m}$  buried oxide (BOX) was deposited with  $1 \mu\text{m}$  of aluminum nitride followed by metallization of  $0.5\text{-}\mu\text{m}$  aluminum (Al) as top electrode [see Fig. 6(a)]. The deposited AlN layer and top Al electrode were patterned subsequently using dry etching with a combination gas of  $\text{Cl}_2/\text{BCl}_3/\text{Ar}$  (in the ratio of 110:60:15) in an Applied Materials (AMAT) Centura Electron Cyclotron Resonance

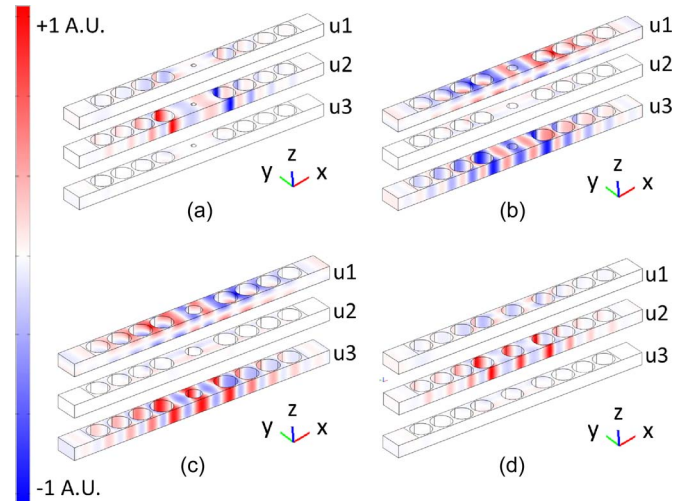


Fig. 4. Simulated mode profiles of displacement of PnC Bloch-mode resonator with  $w = 2a$  and with (a)  $r' = 2 \mu\text{m}$ , (b)  $r' = 4 \mu\text{m}$ , (c)  $r' = 6 \mu\text{m}$ , and (d)  $r' = 8 \mu\text{m}$ . The  $u_1$ ,  $u_2$ , and  $u_3$  represent the displacement vector components in the  $x$ -,  $y$ -, and  $z$ -directions, respectively. The color bar indicates the amplitude of displacements in an arbitrary unit.

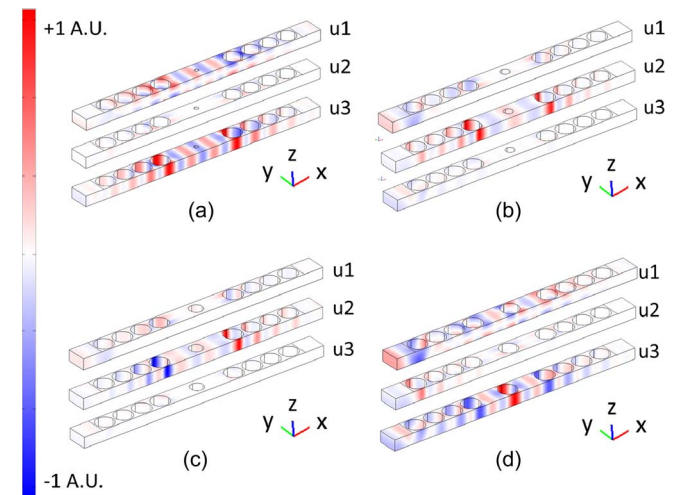


Fig. 5. Simulated mode profiles of displacement of PnC Bloch-mode resonator with  $w = 3a$  and with (a)  $r' = 2 \mu\text{m}$ , (b)  $r' = 4 \mu\text{m}$ , (c)  $r' = 6 \mu\text{m}$ , and (d)  $r' = 8 \mu\text{m}$ . The  $u_1$ ,  $u_2$ , and  $u_3$  represent the displacement vector components in the  $x$ -,  $y$ -, and  $z$ -directions, respectively. The color bar indicates the amplitude of displacements in an arbitrary unit.

etcher (model: 5200; chamber pressure: 11 mT; bias voltage:  $-1000 \text{ V}$ ; RF power: 1300 W), using an endpoint-based recipe to detect etch completion with endpoint detection mechanism, so that overetching of silicon/AlN is minimized. This will form the interdigital transducers (IDTs) which act as the input and output of the acoustic waves on the configured AlN layer [see Fig. 6(b)]. After that, a two-step DRIE is performed, one on the front side and another from the rear side of the wafer, forming cylindrical air holes of the square lattice of PnCs in the silicon device layer [see Fig. 6(c)]. The latter will release the structure from the bulk substrate, resulting in a free-standing 2-D silicon PnC slab. Lastly, the device is fully released by hydrofluoric vapor that etches away the BOX underneath the PnC slab [see Fig. 6(d)]. Fig. 7(a) shows a microfabricated PnC structure of ten periods (rows) of air holes, with IDT formed by Al on the

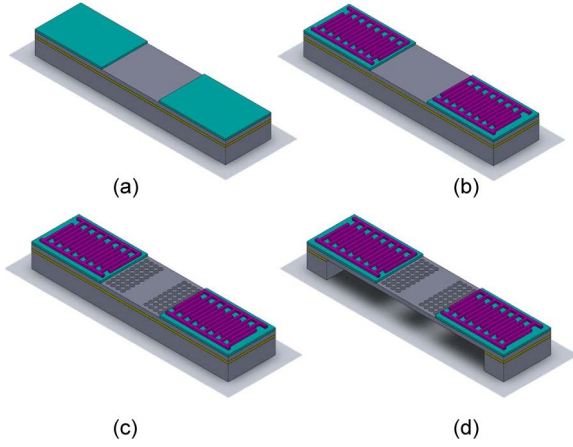


Fig. 6. Fabrication process starting from SOI wafer. (a) AlN deposition and patterning. (b) Top Al electrode deposition and patterning. (c) PnC formation by device layer DRIE. (d) Backside release by DRIE.

two sides of the PnC structure. A closeup view of the PnC structure is shown in Fig. 7(b). Fig. 7(c) and (e) show the PnC Bloch-mode resonators with  $w = 2a$ ,  $r' = 4 \mu\text{m}$  and  $w = 3a$ ,  $r' = 4 \mu\text{m}$ , respectively. Four periods (rows) of air holes are patterned at each side of the defect region for all the PnC Bloch-mode resonators. Fig. 7(d) and (f) shows the closeup view of the central defect region of the PnC Bloch-mode resonators in Fig. 7(c) and (e), respectively. The PnC Bloch-mode resonators with four types of  $r'$ , including 2, 4, 6, and 8  $\mu\text{m}$ , are prepared and characterized in the current study.

#### IV. DEVICE CHARACTERIZATION

To experimentally characterize the microfabricated PnC devices, an Agilent E8364B network analyzer (short-open-load-through calibrated) was used to measure the transmission spectrum against frequency via IDT on the two sides of the PnC devices. Due to the piezoelectric properties of AlN film, acoustic waves were launched toward the PnC structure when an ac signal was applied on the IDT of the input port. The transmission through the PnC structure was picked up by the IDT of the output port. As the bandwidth of the IDT is small and the frequency range of interest is large (from 100 to 240 MHz), 15 sets of transducers with different electrode geometries were fabricated to cover the entire band of interest. We then extracted the  $S_{21}$  parameter which is essentially the transmission of acoustic waves after the interaction with the PnC structure. A free-standing silicon slab without any PnC structure and with the same length is characterized by the same measurement setup such that the wave propagation of the tested PnC devices is normalized with respect to the transmission of the free-standing silicon slab in the same frequency range.

Fig. 8 shows the transmission spectrum of the PnC structure shown in Fig. 7(a). We observed that the measured stopband of  $140 \text{ MHz} < f < 195 \text{ MHz}$  agreed quite well with the simulation results ( $143.8 \text{ MHz} < f < 186.8 \text{ MHz}$ ). We believe the discrepancies are due to the drift of CD control in the microfabrication process, in which the radii of the air holes in microfabricated devices are larger than designed. The measured stopband leads to the center frequency of 167.5 MHz and gap-

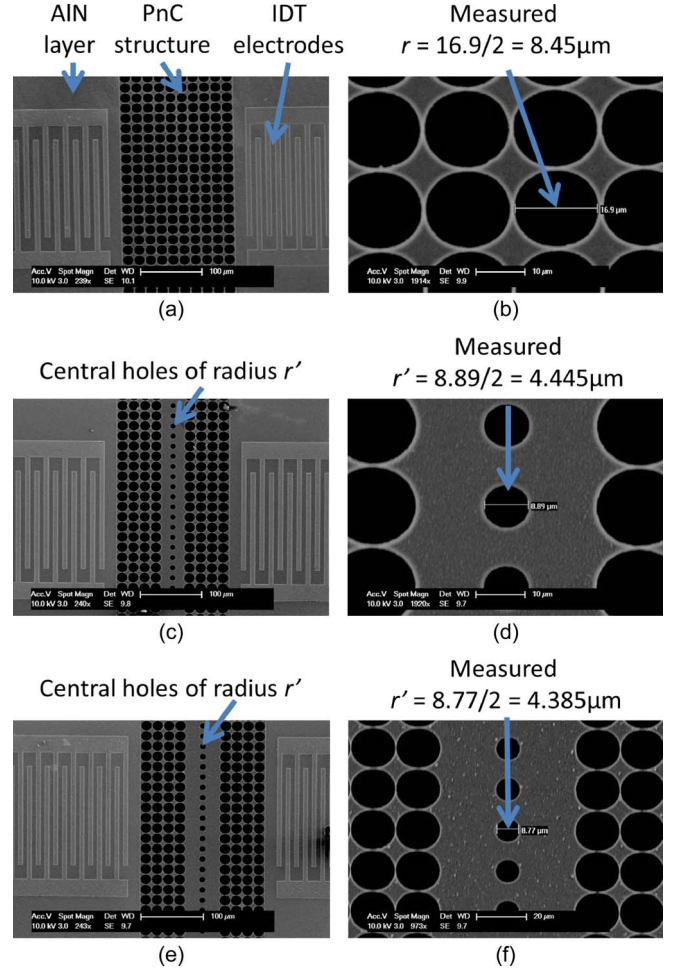


Fig. 7. SEM images of (a) PnC structure, (b) closeup view of the PnC structure, (c) PnC Bloch-mode resonator with  $w = 2a$  and  $r' = 4 \mu\text{m}$ , (d) closeup view of the defect region of the PnC Bloch-mode resonator with  $w = 2a$  and  $r' = 4 \mu\text{m}$ , (e) PnC Bloch-mode resonator with  $w = 3a$  and  $r' = 4 \mu\text{m}$ , and (f) closeup view of the defect region of the PnC Bloch-mode resonator with  $w = 3a$  and  $r' = 4 \mu\text{m}$ .

to-midgap frequency ratio of 32.8%. Fig. 8 also shows a maximum attenuation of 30 dB within the stopband. The large discrepancy in the maximum attenuation between the experimental and the simulated data could be due to two reasons. First, the noise floor in the measurement is high, which is around  $-30 \text{ dB}$ . Signals below that noise floor could not be picked up by the network analyzer. Second, the scattering loss, which is a major source of energy loss, is not considered when periodic boundary conditions were applied in the simulation, and we assumed that the whole resonator is formed by the duplication of the repeating unit in the  $y$ -direction. The scattering loss could reduce the energy confinement by the phononic structure, thus decreasing the maximum transmission attenuation.

Fig. 9 shows the measured transmission spectra of PnC Bloch-mode resonators with  $w = 2a$  and with (a)  $r' = 2 \mu\text{m}$ , (b)  $r' = 4 \mu\text{m}$ , (c)  $r' = 6 \mu\text{m}$ , and (d)  $r' = 8 \mu\text{m}$ . The tested resonant frequency agrees quite well with simulated data. For example, the resonant frequency shown in Fig. 9(b) is 161.25 MHz, and the resonant frequency obtained in Fig. 3(b) is 162.75 MHz. The slight deviation of measured resonant frequency could be due to the variation of the hole size and

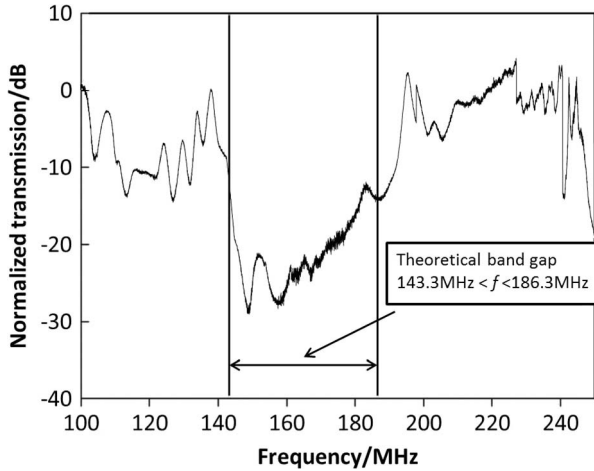


Fig. 8. Measured transmission spectrum of the optimized PnC structure. A stopband of  $140 \text{ MHz} < f < 195 \text{ MHz}$  is obtained, which agrees with the theoretical bandgap shown in Fig. 1 ( $143.3 \text{ MHz} < f < 186.3 \text{ MHz}$ ) very well.

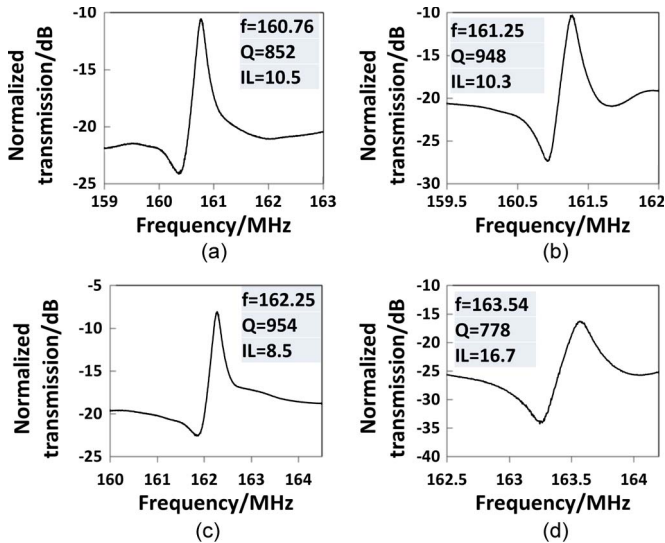


Fig. 9. Measured transmission spectrum of PnC Bloch-mode resonator with  $w = 2a$  and with (a)  $r' = 2 \mu\text{m}$ , (b)  $r' = 4 \mu\text{m}$ , (c)  $r' = 6 \mu\text{m}$ , and (d)  $r' = 8 \mu\text{m}$ .

lattice constant introduced in the microfabrication step. We observed that the resonant frequency increased with respect to the increment of  $r'$ . Moreover, as  $r'$  increases from 2 to  $6 \mu\text{m}$ , Q factor increases gradually from 852 to 954, while Q factor drops to 778 when  $r'$  further increases to  $8 \mu\text{m}$ . It implies that the resonance condition of a Bloch-mode resonator with a central-hole radius of  $8 \mu\text{m}$  is slightly deviated from the optimized condition as achieved in the cases of  $r'$  of 4 and  $6 \mu\text{m}$ . The measured data are in good agreement with the simulated mode profile shown in Fig. 4. The displacement vector components for  $r = 6 \mu\text{m}$  [see Fig. 4(c)] are concentrated at the central defect region, which means that better confinement of energy by the surrounding phononic structure, and thus, higher Q factor was achieved by this design. On the other hand, in the case of  $r' = 8 \mu\text{m}$  where the size of the central holes is comparable to the size of the air holes of the surrounding phononic structure [see Fig. 4(d)], the displacement vector components

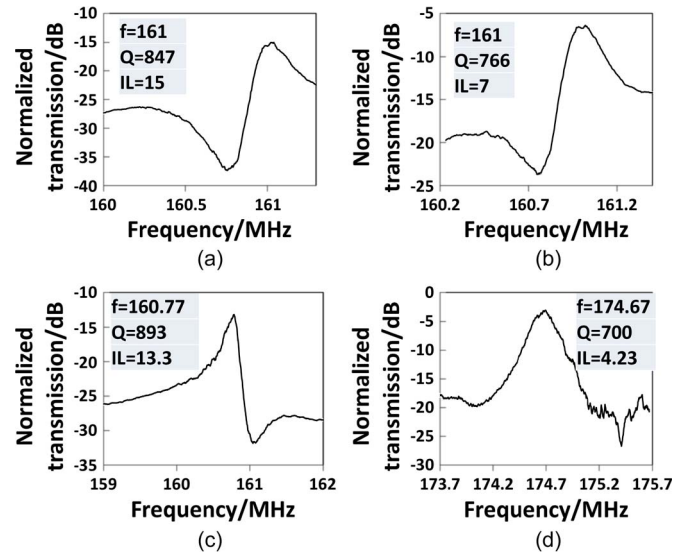


Fig. 10. Measured transmission spectrum of PnC Bloch-mode resonator with  $w = 3a$  and with (a)  $r' = 2 \mu\text{m}$ , (b)  $r' = 4 \mu\text{m}$ , (c)  $r' = 6 \mu\text{m}$ , and (d)  $r' = 8 \mu\text{m}$ .

and, thus, the energy are poorly confined within the central defect region, which leads to a lower measured Q factor of 778 [see Fig. 9(d)].

Fig. 10 shows the measured transmission spectra of the PnC Bloch-mode resonator with  $w = 3a$  and with (a)  $r' = 2 \mu\text{m}$ , (b)  $r' = 4 \mu\text{m}$ , (c)  $r' = 6 \mu\text{m}$ , and (d)  $r' = 8 \mu\text{m}$ . The measured data are in excellent agreement with the modeling results [e.g., 160.77 MHz in Fig. 10(c) versus 160.95 MHz in Fig. 3(c)]. As  $r'$  increases from 2 to  $6 \mu\text{m}$ , the resonant frequency remains relatively constant, which then increases sharply as  $r'$  further increases to  $8 \mu\text{m}$ . This result is consistent with the case of  $w = 2a$ . In addition, as  $r'$  increases from 2 to  $4 \mu\text{m}$ , Q factor drops from 847 to 766, while Q factor rises to 893 when  $r'$  further increases to  $6 \mu\text{m}$ . Upon further increment of  $r'$  to  $8 \mu\text{m}$ , Q factor drops again to only 700. We can see that the optimized condition for Q factor is  $r' = 6 \mu\text{m}$  and this is the same optimized condition for the case of the PnC Bloch-mode resonator with  $w = 2a$ . Again, this leads to a conclusion that the resonance conditions of Bloch-mode resonators with central-hole radii of 4 and  $8 \mu\text{m}$  are slightly deviated from the optimized condition as achieved in the cases of  $r'$  of  $6 \mu\text{m}$ . Also, the measured data confirm the simulated mode profiles of displacement shown in Fig. 5. The displacement vector components for  $r' = 6 \mu\text{m}$  [see Fig. 5(c)] are more concentrated at the central defect region than other designs, which means the best confinement of the energy by the surrounding phononic structure, while for the cases of  $r' = 4 \mu\text{m}$  [see Fig. 5(b)] and  $r' = 8 \mu\text{m}$  [see Fig. 5(d)], the displacement vectors are large at one end of the structure and then distributed almost evenly along the structure, which yield poor confinement of energy by the surrounding phononic structure and, thus, lower Q factors.

The Q factors for all eight designs of resonators are summarized in Table I. Although the trend of Q factor as  $r'$  increases for the PnC Bloch-mode resonator with  $w = 2a$  is different from the case of  $w = 3a$ , the optimized conditions for the two types of resonator are the same, i.e., Q factor reaches

TABLE I  
Q FACTORS FOR ALL EIGHT DESIGNS OF RESONATORS

$r'$ ( $\mu\text{m}$ ) \backslash $w(a)$	2	4	6	8
2	852	948	954	778
3	847	766	893	700

maximum when  $r' = 6 \mu\text{m}$ . Moreover, the resonant frequencies for both types of resonators reaches their individual maximum at  $r' = 8 \mu\text{m}$ . Thus, we can conclude that the Q factor reaches maximum when  $r' = 6 \mu\text{m}$  and the resonant frequency reaches maximum when  $r' = 8 \mu\text{m}$  for the type of PnC Bloch-mode resonators with several central rows of air holes removed and replaced with only one row of air holes on a 2-D PnC of square lattice. When putting both types of resonators under their respective optimized condition ( $r' = 6 \mu\text{m}$  for Q factor and  $r' = 8 \mu\text{m}$  for resonant frequency), the PnC Bloch-mode resonator with  $w = 2a$  has lower resonant frequency and higher Q factor.

Mohammadi *et al.* have reported a cavity-mode-based PnC resonator using a 2-D silicon PnC slab of hexagonal lattice [31]. Two kinds of resonant peaks were reported. One type of resonant peak with Q factor of 680 and IL of 4.6 dB was obtained at 149.5 MHz, and the other type of resonant peak with Q factor of 6300 and IL of 21 dB was obtained at 126.52 MHz. Due to the nature of better confinement of acoustic waves and four rows of air holes in one period, the cavity-mode resonator of hexagonal lattice using three periods provides resonance of higher Q factor with compromise of higher IL. In the case of the cavity-mode resonator using two periods, i.e., eight rows of air holes, resonant peak of lower Q factor and lower IL was obtained. In the current study, four periods, i.e., four rows of air holes, are employed for all Bloch-mode PnC resonators of square lattice. Although the acoustic wave confinement of PnC structures of square lattice is not as good as the one of hexagonal lattice, the measured Q factor of characterized Bloch-mode PnC resonators of square lattice with four rows of air holes is slightly better than the Q factor of the cavity-mode PnC resonators with eight rows of air holes. This is because propagating waves inside the PnCs are a set of solutions of the wave equations satisfying the translational symmetry property. However, in finite periodic media where point defects are introduced to break the translational symmetry, evanescent modes can be supported as well. Recently, Laude *et al.* have analyzed the evanescent Bloch waves and the complex band structure of PnC [42]. In the complex band structure, band can be shown where this is not the case when one uses traditional  $\omega(k)$  method to solve the band structure. By including the complex band structure, bandgaps can be defined as ranges of frequencies where all Bloch waves have to be evanescent [43]. For the case of cavity-mode PnC resonator, acoustic waves are of cavity-mode in the defect region (cavity region) while acoustic waves are of Bloch-mode in the PnC structure surrounding the defect region. The conversion between the two modes comes with substantial amount of energy loss due to the mismatch in acoustic impedance of these two modes. However, in the case of Bloch-mode resonators, the acoustic waves in both the PnC structure and the defect region are of Bloch-mode.

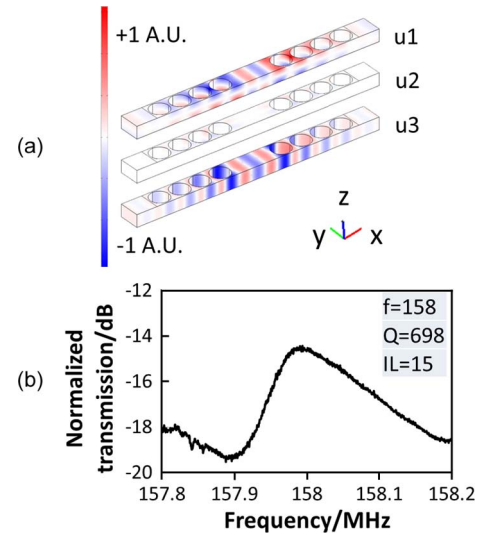


Fig. 11. (a) Simulated mode profiles of displacement of PnC cavity-mode resonator with  $w = 2a$ . (b) Measured transmission spectrum of PnC cavity-mode resonator with  $w = 2a$ .

This means that only slight mode conversion is involved when acoustic waves are confined within the defect region; thus, less energy is lost, and higher Q factor can be achieved. As a result, for similar design of Bloch-mode PnC resonators of square lattice using more periods, we can expect to get resonant peak of higher Q factor with slightly increased IL. Also, since the measured Q factor of the proposed Bloch-mode PnC resonators of square lattice with four rows of air holes is slightly better than the Q factor of the cavity-mode PnC resonators with eight rows of air holes, smaller device area is another advantage of the proposed Bloch-mode resonator as compared to other cavity-mode resonators.

In order to clarify the physical picture of the difference between the mode shapes of cavity mode and Bloch mode, a Fabry-Perot cavity-mode resonator (without any air holes at the center of the cavity and with  $w = 2a$ ) was also analyzed numerically and experimentally. The simulated mode profiles of displacement and the experimentally measured transmission spectrum are shown in Fig. 11(a) and (b), respectively. Fig. 11(a) shows the typical Fabry-Perot resonant modes: the elastic energy is uniformly concentrated at the central defect region, and the polarizations are in  $x$ - and  $z$ -directions. The mode is quite similar to the flexural mode of the Lamb wave. However, in Fig. 4, when air holes are added into the center of the cavity, there are some polarization in the  $y$ -direction, particularly for the cases of Fig. 4(a) and (d), whereby polarization is concentrated in the  $y$ -direction. In addition, two kinds of oscillating modes appear in the cavity at the same time. First, the largest displacement is observed at the inner edges of the cavity. Second, we can observe that some elastic energy penetrates through the cavity. The former mode is analogous to the second localized mode of locally resonant sonic materials in [44]. The material consists of metal lead balls with silicon rubber coating embedded in epoxy matrix. For the second localized mode, the largest displacement appears in the silicon rubber. Similar localized modes have been observed in several localized resonant materials [45], [46]. For the Bloch-mode

resonators whereby air holes are added into the center of the cavity, the Lamb-wave mode within the cavity is destroyed by the presence of the central air holes. From Fig. 4, one can see that, unlike the case in Fig. 11(a), the elastic energy is no longer uniformly concentrated at the central defect region. Instead, there is more elastic energy in the region of added air holes. This phenomenon becomes more obvious when  $r'$  increases. The cavity turns into an oscillator which consists of a mass clamped by the PnC structures on both sides. Hence, part of the incident elastic energy excites the second localized mode, while another part of the energy excites the new propagating mode. The propagating mode is polarized in the  $y$ -direction and reflected back and forth within the cavity by the PnC structure surrounding the cavity. It is equivalent to the nonresonant propagating mode which passes through the periodic oscillator array.

From the measured transmission spectrum of the cavity-mode resonator shown in Fig. 11(b), we can see that the Q factor is 698, which is slightly less than the Q factors of the Bloch-mode resonators in Table I. This agrees with the simulated mode profiles of displacement for both types of resonators. As both types of resonators were fabricated under the same processing conditions, the measured transmission spectra confirm that, by having air holes at the center of the cavity, mode mismatch can be reduced and Q factor can be improved.

## V. CONCLUSION

In this paper, development work of the PnC resonators based on Bloch-mode resonance for 2-D PnC structures has been explored and characterized. Experimental data for eight designs of PnC Bloch-mode resonators which belong to two different types of cavity width ( $w$ ) based on square lattice PnC structure were reported. These designed PnC Bloch-mode resonators of square lattice were realized from a microfabricated free-standing silicon plate. We have also characterized these two types of resonators with different central-hole radii ( $r'$ ) to explore the effect of  $r'$  and  $w$  on resonant frequency and Q factor. Preliminary data show that, for our fabricated PnC Bloch-mode resonators with central rows of air holes removed and replaced with one row of air holes on a 2-D PnC of square lattice, the Q factor reaches maximum when  $r' = 6 \mu\text{m}$  and the resonant frequency reaches maximum when  $r' = 8 \mu\text{m}$ . In addition, with relatively smaller PnC active area than other reported designs, the Bloch-mode PnC resonators based on square lattice PnC structure are very promising to be further explored for various applications such as microfluidics, biomedical devices, and RF communications.

## REFERENCES

- [1] H. M. Lavanani, R. Abdolvand, and F. Ayazi, "A 500 MHz low phase-noise AlN-on-silicon reference oscillator," in *Proc. IEEE CICC*, 2007, pp. 599–602.
- [2] S. Ryder, K. B. Lee, X. F. Meng, and L. W. Lin, "AFM characterization of out-of-plane high frequency microresonators," *Sens. Actuators A, Phys.*, vol. 114, no. 2, pp. 135–140, Sep. 2004.
- [3] D. Joachim and L. Liwei, "Characterization of selective polysilicon deposition for MEMS resonator tuning," *J. Microelectromech. Syst.*, vol. 12, no. 2, pp. 193–200, Apr. 2003.
- [4] L. Khine and M. Palaniapan, "High-Q bulk-mode SOI square resonators with straight-beam anchors," *J. Micromech. Microeng.*, vol. 19, no. 1, p. 015 017, Jan. 2009.
- [5] K. Wang, A. C. Wong, and C. T. C. Nguyen, "VHF free-free beam high-Q micromechanical resonators," *J. Microelectromech. Syst.*, vol. 9, no. 3, pp. 347–360, Sep. 2000.
- [6] L. Yu-Wei, L. Sheng-Shian, X. Yuan, R. Zeying, and C. T. C. Nguyen, "Vibrating micromechanical resonators with solid dielectric capacitive transducer gaps," in *Proc. IEEE Int. Freq. Control Symp. Expo.*, 2005, pp. 128–134.
- [7] S. Pourkamali, A. Hashimura, R. Abdolvand, G. K. Ho, A. Erbil, and F. Ayazi, "High-Q single crystal silicon HARPSS capacitive beam resonators with self-aligned sub-100-nm transduction gaps," *J. Microelectromech. Syst.*, vol. 12, no. 4, pp. 487–496, Aug. 2003.
- [8] G. K. Ho, R. Abdolvand, A. Sivapurapu, S. Humad, and F. Ayazi, "Piezoelectric-on-silicon lateral bulk acoustic wave micromechanical resonators," *J. Microelectromech. Syst.*, vol. 17, no. 2, pp. 512–520, Apr. 2008.
- [9] G. Piazza, P. J. Stephanou, and A. P. Pisano, "Piezoelectric aluminum nitride vibrating contour-mode MEMS resonators," *J. Microelectromech. Syst.*, vol. 15, no. 6, pp. 1406–1418, Dec. 2006.
- [10] G. Piazza, P. J. Stephanou, and A. P. Pisano, "Single-chip multiple-frequency AlN MEMS filters based on contour-mode piezoelectric resonators," *J. Microelectromech. Syst.*, vol. 16, no. 2, pp. 319–328, Apr. 2007.
- [11] C. T. C. Nguyen, "MEMS technology for timing and frequency control," *IEEE Trans. Ultrason., Ferroelectr., Freq. Control*, vol. 54, no. 2, pp. 251–270, Feb. 2007.
- [12] R. H. Olsson and I. El-Kady, "Microfabricated phononic crystal devices and applications," *Meas. Sci. Technol.*, vol. 20, no. 1, p. 012002, Jan. 2009.
- [13] S. Benchabane, A. Khelif, J. Y. Rauch, L. Robert, and V. Laude, "Evidence for complete surface wave band gap in a piezoelectric phononic crystal," *Phys. Rev. E*, vol. 73, no. 6, p. 065601, Jun. 2006.
- [14] I. El-Kady, R. H. Olsson, and J. G. Fleming, "Phononic band-gap crystals for radio frequency communications," *Appl. Phys. Lett.*, vol. 92, no. 23, pp. 233 504-1–233 504-3, Jun. 2008.
- [15] S. Mohammadi, A. A. Eftekhar, A. Khelif, W. D. Hunt, and A. Adibi, "Evidence of large high frequency complete phononic band gaps in silicon phononic crystal plates," *Appl. Phys. Lett.*, vol. 92, no. 22, pp. 221 905-1–221 905-3, Jun. 2008.
- [16] S. Mohammadi, A. A. Eftekhar, A. Khelif, H. Moubchir, R. Westafer, W. D. Hunt, and A. Adibi, "Complete phononic bandgaps and bandgap maps in two-dimensional silicon phononic crystal plates," *Electron. Lett.*, vol. 43, no. 16, pp. 898–899, Aug. 2007.
- [17] T. T. Wu, L. C. Wu, and Z. G. Huang, "Frequency band-gap measurement of two-dimensional air/silicon phononic crystals using layered slanted finger interdigital transducers," *J. Appl. Phys.*, vol. 97, no. 9, pp. 094916-1–094916-7, May 2005.
- [18] F.-L. Hsiao, A. Khelif, H. Moubchir, A. Choujaa, C.-C. Chen, and V. Laude, "Waveguiding inside the complete band gap of a phononic crystal slab," *Phys. Rev. E*, vol. 76, no. 5, pp. 056601-1–056601-6, Nov. 2007.
- [19] R. H. Olsson, I. F. El-Kady, M. F. Su, M. R. Tuck, and J. G. Fleming, "Microfabricated VHF acoustic crystals and waveguides," *Sens. Actuators A, Phys.*, vol. 145/146, pp. 87–93, Jul./Aug. 2008.
- [20] K. Nai-Kuei, Z. Chengjie, and G. Piazza, "Demonstration of inverse acoustic band gap structures in AlN and integration with piezoelectric contour mode wideband transducers," in *Proc. IEEE Int. Freq. Control Symp. Joint 22nd Eur. Freq. Time Forum*, 2009, pp. 10–13.
- [21] M. F. Su, R. H. Olsson, Z. C. Leseman, and I. El-Kady, "Realization of a phononic crystal operating at gigahertz frequencies," *Appl. Phys. Lett.*, vol. 96, no. 5, pp. 053111-1–053111-3, Feb. 2010.
- [22] Y. M. Soliman, M. F. Su, Z. C. Leseman, C. M. Reinke, I. El-Kady, and R. H. Olsson, "Phononic crystals operating in the gigahertz range with extremely wide band gaps," *Appl. Phys. Lett.*, vol. 97, no. 19, pp. 193 502-1–193 502-3, Nov. 2010.
- [23] J. O. Vasseur, A. C. Hladky-Hennion, B. Djafari-Rouhani, F. Duval, B. Dubus, Y. Pennec, and P. A. Deymier, "Waveguiding in two-dimensional piezoelectric phononic crystal plates," *J. Appl. Phys.*, vol. 101, no. 11, pp. 114 904-1–114 904-6, Jun. 2007.
- [24] S. Benchabane, A. Khelif, A. Choujaa, B. Djafari-Rouhani, and V. Laude, "Interaction of waveguide and localized modes in a phononic crystal," *Europhys. Lett.*, vol. 71, no. 4, pp. 570–575, Aug. 2005.
- [25] A. Khelif, P. A. Deymier, B. Djafari-Rouhani, J. O. Vasseur, and L. Dobrzynski, "Two-dimensional phononic crystal with tunable narrow

pass band: Application to a waveguide with selective frequency," *J. Appl. Phys.*, vol. 94, no. 3, pp. 1308–1311, Aug. 2003.

- [26] A. Khelif, A. Choujaa, B. Djafari-Rouhani, M. Wilm, S. Ballandras, and V. Laude, "Trapping and guiding of acoustic waves by defect modes in a full-band-gap ultrasonic crystal," *Phys. Rev. B*, vol. 68, no. 21, pp. 214 301-1–214 301-4, Dec. 2003.
- [27] A. Khelif, S. Mohammadi, A. A. Eftekhar, A. Adibi, and B. Aoubiza, "Acoustic confinement and waveguiding with a line-defect structure in phononic crystal slabs," *J. Appl. Phys.*, vol. 108, no. 8, pp. 084515-1–084515-5, Oct. 2010.
- [28] S. Mohammadi, A. A. Eftekhar, and A. Adibi, "Support loss-free micro/nano-mechanical resonators using phononic crystal slab waveguides," in *Proc. IEEE Int. FCS*, 2010, pp. 521–523.
- [29] M. Oudich, M. B. Assouar, and Z. Hou, "Propagation of acoustic waves and waveguiding in a two-dimensional locally resonant phononic crystal plate," *Appl. Phys. Lett.*, vol. 97, no. 19, pp. 193 503-1–193 503-3, Nov. 2010.
- [30] Y. W. Gu, X. D. Luo, and H. R. Ma, "Low frequency elastic wave propagation in two dimensional locally resonant phononic crystal with asymmetric resonator," *J. Appl. Phys.*, vol. 105, no. 4, pp. 044903-1–044903-7, Feb. 2009.
- [31] S. Mohammadi, A. A. Eftekhar, W. D. Hunt, and A. Adibi, "High-Q micromechanical resonators in a two-dimensional phononic crystal slab," *Appl. Phys. Lett.*, vol. 94, no. 5, pp. 051 906-1–051 906-3, Feb. 2009.
- [32] K. Nai-Kuei and G. Piazza, "Evidence of acoustic wave focusing in a microscale 630 MHz aluminum nitride phononic crystal waveguide," in *Proc. IEEE Int. FCS*, 2010, pp. 530–533.
- [33] M. W. McCutcheon and M. Loncar, "Design of a silicon nitride photonic crystal nanocavity with a quality factor of one million for coupling to a diamond nanocrystal," *Opt. Exp.*, vol. 16, no. 23, pp. 19 136–19 145, Nov. 2008.
- [34] P. Lalanne and J. P. Hugonin, "Bloch-wave engineering for high-Q, small-V microcavities," *IEEE J. Quantum Electron.*, vol. 39, no. 11, pp. 1430–1438, Nov. 2003.
- [35] C. Sauvan, G. Lecamp, P. Lalanne, and J. P. Hugonin, "Modal-reflectivity enhancement by geometry tuning in photonic crystal microcavities," *Opt. Exp.*, vol. 13, no. 1, pp. 245–255, Jan. 2005.
- [36] S. Lee, J. Thillaigovindan, C. C. Chen, X. T. Chen, Y. T. Chao, S. H. Tao, W. F. Xiang, A. B. Yu, H. H. Feng, and G. Q. Lo, "Si nanophotonics based cantilever sensor," *Appl. Phys. Lett.*, vol. 93, no. 11, pp. 113 113-1–113 113-3, Sep. 2008.
- [37] S. Lee, R. Radhakrishnan, C. C. Chen, J. Li, J. Thillaigovindan, and N. Balasubramanian, "Design and modeling of a nanomechanical sensor using silicon photonic crystals," *J. Lightw. Technol.*, vol. 26, no. 7, pp. 839–846, Apr. 2008.
- [38] P. B. Deotare, M. W. McCutcheon, I. W. Frank, M. Khan, and M. Loncar, "High quality factor photonic crystal nanobeam cavities," *Appl. Phys. Lett.*, vol. 94, no. 12, pp. 121 106-1–121 106-3, Mar. 2009.
- [39] J. Jagerska, H. Zhang, Z. L. Diao, N. Le Thomas, and R. Houdre, "Refractive index sensing with an air-slot photonic crystal nanocavity," *Opt. Lett.*, vol. 35, no. 15, pp. 2523–2525, Aug. 2010.
- [40] B. W. Wang, M. A. Dundar, R. Notzel, F. Karouta, S. L. He, and R. W. van der Heijden, "Photonic crystal slot nanobeam slow light waveguides for refractive index sensing," *Appl. Phys. Lett.*, vol. 97, no. 15, pp. 151 105-1–151 105-3, Oct. 2010.
- [41] A. Di Falco, L. O'Faolain, and T. F. Krauss, "Dispersion control and slow light in slotted photonic crystal waveguides," *Appl. Phys. Lett.*, vol. 92, no. 8, pp. 083501-1–083501-3, Feb. 2008.
- [42] V. Laude, Y. Achaoui, S. Benhabane, and A. Khelif, "Evanescence Bloch waves and the complex band structure of phononic crystals," *Phys. Rev. B*, vol. 80, no. 9, p. 092301, Sep. 2009.
- [43] V. Romero-Garcia, J. V. Sanchez-Perez, S. Castineira-Ibanez, and L. M. Garcia-Raffi, "Evidences of evanescent Bloch waves in phononic crystals," *Appl. Phys. Lett.*, vol. 96, no. 12, pp. 124 102-1–124 102-3, Mar. 2010.
- [44] Z. Y. Liu, X. X. Zhang, Y. W. Mao, Y. Y. Zhu, Z. Y. Yang, C. T. Chan, and P. Sheng, "Locally resonant sonic materials," *Science*, vol. 289, no. 5485, pp. 1734–1736, Sep. 2000.
- [45] M. Hirsekorn, "Small-size sonic crystals with strong attenuation bands in the audible frequency range," *Appl. Phys. Lett.*, vol. 84, no. 17, pp. 3364–3366, Apr. 2004.
- [46] C. Goffaux and J. Sanchez-Dehesa, "Two-dimensional phononic crystals studied using a variational method: Application to lattices of locally resonant materials," *Phys. Rev. B*, vol. 67, no. 14, pp. 144 301-1–144 301-10, Apr. 2003.



**Nan Wang** (S'11) received the B.Eng. degree from the Department of Electrical and Computer Engineering, National University of Singapore, Singapore, in 2009, where he is currently working toward the Ph.D. degree and is attached to the Institute of Microelectronics, Agency for Science, Technology and Research, Singapore.

His research interests include radio-frequency MEMS and phononic crystals.

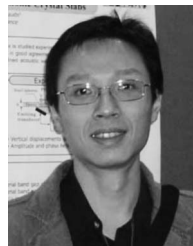


**Julius Ming-Lin Tsai** was born in Taipei, Taiwan, in June 1976. He received the B.S. and Ph.D. degrees in power mechanical engineering from National Tsing Hua University, Hsinchu, Taiwan, in 1995 and 2004, respectively.

From June 2003 to April 2004, he was a Visiting Scholar at Carnegie-Mellon University, Pittsburgh, PA, where he was involved with low-noise CMOS accelerometers. From 2004 to 2009, he was with VIA Technologies, where he was involved with high-frequency small-signal modeling.

He is currently a Principle Investigator in the Institute of Microelectronics, Singapore, Singapore, and an Adjunct Assistant Professor in the Department of Electrical and Computer Engineering, National University of Singapore, Singapore. His main research interests are in radio-frequency MEMS, nanoelectromechanical system switches, MEMS ultrasound transducers, and ruggedized MEMS sensors.

Dr. Tsai was the recipient of a scholarship presented by the National Science Council of Taiwan.



**Fu-Li Hsiao** received the B.S. degree from the Department of Physics, National Changhua University of Education, Changhua, Taiwan, in 2002, and the Ph.D. degree jointly from FEMTO-ST of the University of Franche-Comte, Besançon, France, and the Department of Optics and Photonics, National Central University, Jhongli City, Taiwan, in 2008.

He was a Research Fellow in the Department of Electrical and Computer Engineering, National University of Singapore, Singapore, from 2008 to 2009. He is currently an Assistant Professor with the Graduate Institute of Photonics, National Changhua University of Education, Taiwan, and also a visiting scholar in the Department of Electrical and Computer Engineering, National University of Singapore, Singapore. His current research interests include photonic crystals, phononic crystals, mechanical resonators, and optical MEMS.



**Bo Woon Soon** received the B.Eng. degree in microelectronics from Liverpool John Moores University, Liverpool, U.K., in 2006. He is currently working toward the M.Eng. degree in the Department of Electrical and Computer Engineering, National University of Singapore, Singapore.

He is currently a Research Engineer in the Department of Sensors and Actuator Microsystems of the Institute of Microelectronics, Agency for Science, Technology and Research, Singapore. His research interests are MEMS integration processes, nano-electromechanical system switches, and ruggedized MEMS.



**Dim-Lee Kwong** (F'09) received the B.S. degree in physics and the M.S. degree in nuclear engineering from National Tsing Hua University, Hsinchu, Taiwan, in 1977 and 1979, respectively. He received the Ph.D. degree in electrical engineering from Rice University, Houston, TX, in 1982.

He is the Executive Director of the Institute of Microelectronics (IME), Agency for Science, Technology and Research, Singapore, a Professor of electrical and computer engineering with the National University of Singapore, Singapore, and an

Adjunct Professor of electrical and computer engineering with the University of Texas at Austin. He was the Earl N. and Margaret Bransfield Endowed Professor with the University of Texas at Austin from 1990 to 2007 and the Temasek Professor with the National University of Singapore from 2001 to 2004. He is the author of more than 1000 refereed archival publications (560 journal and 470 conference proceedings), has presented more than 80 invited talks at international conferences, and is the holder of more than 25 U.S. patents. He was the Founder of Rapro Technology Inc., in 1986, and Micro Integration Corporation, in 1988, and has been a Consultant to government research laboratories, semiconductor IC manufacturers, and materials and equipment suppliers in the U.S. and overseas. More than 55 students received their Ph.D. degrees under his supervision. As an Executive Director of IME, he develops and implements IME's multidisciplinary and multifaceted R&D strategy and research programs that are substantially driven by commercial applications as the end goal. He leads interdisciplinary teams of semiconductor technology, photonics, bioscience, radio frequency and mixed-signal IC design, and advanced packaging, together with strategic industrial and clinical partners, to develop leading-edge disruptive technologies for Si photonics, green electronics, 3-D IC, microelectromechanical systems, and biomedical applications.

Prof. Kwong was the recipient of the IBM Faculty Award from 1984 to 1986, the Semiconductor Research Corporation Inventor Awards from 1993 to 1994, the General Motor Foundation Fellowship from 1992 to 1995, the Halliburton Foundation Excellent Teaching Award in 1994, the Engineering Foundation Award in 1995, the IEEE George Smith Award in 2007, and the 2011 IEEE Frederik Philips Award with the following citation: "For leadership in silicon technology and excellence in the management of microelectronics R&D."



**Moorthi Palaniapan** (M'96) received the B.Eng. (with first class honors) and M.Eng. degrees in electrical engineering from the National University of Singapore, Singapore, in 1995 and 1997, respectively, and the Ph.D. degree from the Department of Electrical Engineering and Computer Sciences, University of California, Berkeley, in 2002.

He is currently an Assistant Professor with the Department of Electrical and Computer Engineering, National University of Singapore. His research interests include integrated microelectromechanical

sensors, actuators, resonator designs, power electronic circuits, biosensors, and nanomechanical graphene sensors.



**Chengkuo Lee** (M'96) received the M.S. degree in materials science and engineering from National Tsing Hua University, Hsinchu, Taiwan, in 1991, the M.S. degree in industrial and system engineering from Rutgers University, New Brunswick, NJ, in 1993, and the Ph.D. degree in precision engineering from The University of Tokyo, Tokyo, Japan, in 1996.

He worked as a Foreign Researcher in the Nanometer-scale Manufacturing Science Laboratory of the Research Center for Advanced Science and

Technology, The University of Tokyo, from 1993 to 1996. He had also worked in the Mechanical Engineering Laboratory, Advanced Industrial Science and Technology (AIST), Ministry of International Trade and Industry (MITI), Tsukuba, Japan, as a Japan Science and Technology Agency (JST) Research Fellow, in 1996. Thereafter, he became a Senior Research Staff Member of the Microsystems Laboratory, Industrial Technology Research Institute, Hsinchu. In September 1997, he joined Metrodyne Microsystem Corporation, Hsinchu, and established the MEMS device division and the first micromachining laboratory for commercial purposes in Taiwan. He was the Manager of the MEMS device division between 1997 and 2000. He was an Adjunct Assistant Professor in the Electrophysics Department of National Chiao Tung University, Hsinchu, in 1998, and an Adjunct Assistant Professor in the Institute of Precision Engineering of National Chung Hsing University, Taichung, Taiwan, from 2001 to 2005. In August 2001, he cofounded Asia Pacific Microsystems, Inc., where he first became Vice President of R&D before becoming Vice President of the optical communication business unit and Special Assistant to the Chief Executive Officer in charge of international business and technical marketing for the MEMS foundry service. From 2006 to 2009, he was a Senior Member of the Technical Staff at the Institute of Microelectronics, Agency for Science, Technology and Research, Singapore. He has been an Assistant Professor in the Department of Electrical and Computer Engineering, National University of Singapore, Singapore, since December 2005. He is the coauthor of *Advanced MEMS Packaging* (McGraw-Hill, 2010). He has contributed to more than 140 international conference papers and extended abstracts and 90 peer-reviewed international journal articles in the fields of sensors, actuators, energy harvesting, nanoelectromechanical systems, nanophotonics, and nanotechnology. He is also the holder of nine U.S. patents.